Materials & Design 223 (2022) 111172

Contents lists available at ScienceDirect

Materials & Design

journal homepage: www.elsevier.com/locate/matdes

Influence of process parameters on the particle–matrix interaction of WC-Co metal matrix composites produced by laser-directed energy deposition

Marta Ostolaza [a,*], Jon Iñaki Arrizubieta [a], Antoine Queguineur [b], Kati Valtonen [c], Aitzol Lamikiz [a], Iñigo Flores Ituarte [b]

[a] Dept. of Mechanical Engineering, University of the Basque Country (UPV/EHU), Torres Quevedo, 1, 48013 Bilbao, Spain
[b] Automation Technology and Mechanical Engineering, Faculty of Engineering and Natural Sciences, Tampere University, Korkeakoulunkatu, 6, FI-33720 Tampere, Finland
[c] Materials Science and Environmental Engineering, Faculty of Engineering and Natural Sciences, Tampere University, Korkeakoulunkatu, 6, FI-33720 Tampere, Finland

HIGHLIGHTS

- The metal-ceramic interaction during the manufacturing of Metal Matrix Composites is thermally driven; thus, it depends on the thermal cycle and process parameters.
- In laser-directed energy deposition of Co-base and WC-reinforced Metal Matrix Composites, diffusion and carbide precipitation are revealed by SEM and EDS analysis.
- The main strengthening mechanisms of Co-WC Metal Matrix Composites are identified: solid-solution of tungsten and carbide precipitation, or grain refinement.
- Statistical regression models are implemented as a tool for data analysis.

GRAPHICAL ABSTRACT

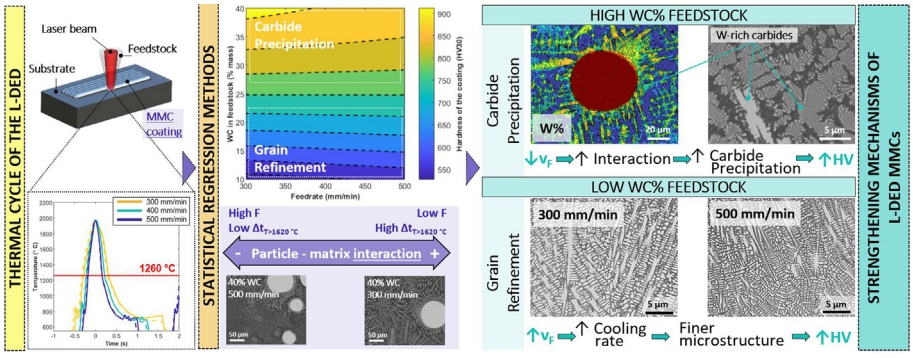

ARTICLE INFO

Article history:
Received 18 July 2022
Revised 1 September 2022
Accepted 17 September 2022
Available online 18 September 2022

Keywords:
Multi-material L-DED
Metal Matrix Composites
Diffusion
Wear-resistant coating
Tungsten carbide
Cobalt-base alloy

ABSTRACT

The prediction of the in-service behaviour of metal-matrix composites produced by laser-directed energy deposition is a fundamental challenge in additive manufacturing. The interaction between the reinforcement phase and the matrix has a major impact on the micro and macroscopic properties of these materials. This interaction is fostered by the exposition of the materials to high temperatures. Hence, it is highly influenced by the thermal cycle of the manufacturing process. In this work, an experimental approach is adopted to determine the influence of the main process parameters on the properties of metal-matrix composites. Statistical regression models are employed to consider the role of the most relevant parameters, from exploration to exploitation. The obtained trends are further corroborated by the corresponding microstructural, SEM, and EDS analyses. In terms of surface hardness, the DOE reveals different trends of the response depending on the composition of the feedstock employed. It is concluded that the strengthening behaviour of the material varies throughout the experimental domain studied. When high WC% feedstocks are employed, the main strengthening mechanism responsible for the increase of hardness is the solid-solution of tungsten and carbide precipitation. On the contrary, when low WC%s are employed, grain refinement becomes the main strengthening mechanism.

* Corresponding author.
E-mail address: marta.ostolaza@ehu.eus (M. Ostolaza).

https://doi.org/10.1016/j.matdes.2022.111172
0264-1275/

1. Introduction

The wear and corrosion of highly loaded surfaces hinder the efficient operation of an extensive range of systems in the industry. Holmberg and Erdemir [1] estimated that even a 40 % reduction of the energy losses due to friction and wear could be attained if novel materials and technologies for surface enhancement were to be implemented in the industry. The development of advanced wear mitigation tools is of utmost importance in today's industrial paradigm, where sustainability and the deployment of reliable and durable systems play a key role [2]. Surface coatings have been widely reported as effective tools for enhancing the surface performance of parts under critical operating conditions or severe environments [3]. Owing to the raise of Additive Manufacturing (AM), new surface modification technologies have become readily available for industrial use, e.g. laser-directed energy deposition (L-DED).

Although first developed for the purpose of rapid manufacturing of prototypes and tooling, L-DED is currently becoming more focused on repair and coating applications. L-DED has already been put into practical use, mainly in the aerospace and automotive industries [4,5]. As far as surface modification is concerned, L-DED has the ability to produce fully dense coatings, which are metallurgically bonded to the substrate or base component [6]. This leads to higher-quality bonds as compared to other traditionally employed surface modification technologies, such as thermal spray [7]. Additionally, L-DED is known to have a very localized and precise control of the energy input, resulting in minimal thermal affection of the substrate and low distortion [8]. Consequently, it is better suited to repair and coat high-added-value components without causing damage to the underlying region [9]. Wear and corrosion-resistant coatings can be fabricated by L-DED, as it permits the deposition of a wide range of metals and alloys. Particularly, hardfacing with Fe-, Ni-, and Co-base alloys has been broadly investigated [8,10]. In this manner, the site-specific performance of highly demanded surfaces can be substantially improved by the deposition of high-performance coatings [11]. Furthermore, a unique feature of the L-DED process, which places this technology in a highly competitive position for materials development and research, is its ability for in-situ production of multi-material structures [12,13].

Owing to the high cooling rates inherent to the thermal cycle of materials manufactured by L-DED, the non-equilibrium synthesis of advanced materials can be carried out, which broadens the scope for the development of novel material systems and multi-material structures [12]. In this context, composite material production and engineered alloy manufacturing have been investigated [14–16]. In fact, the multi-material ability unlocks a series of opportunities such as the development of hybrid materials, the manufacturing of graded structures with tailored material properties or Functionally Graded Materials (FGM), or the fabrication of high-performance Metal Matrix Composite (MMC) coatings for wear- and erosion-resistant applications. In 1991, MMCs were already identified as a suitable solution for the surface modification of components exposed to severe erosion and wear conditions [17]. It has been extensively reported in the literature that these multi-material structures are suitable for aerospace [12], die and mould [18], agricultural [19,20], mining [21], or oil and gas applications [6]. However, their production was strongly limited by the processing techniques available at the time, as their manufacture by conventional methods is complicated [22]. In the last decade, and owing to the rise of AM technologies, namely, L-DED, a significant effort is being invested in the research of this topic.

For instance, Zhang and Kovacevic [6], Nurminen et al. [23], and Adam et al. [24], studied different matrix and reinforcement materials, and they compared the microstructure generated and the mechanical properties achieved in each case. As far as the metal matrix is concerned, when high temperatures are to be withstood, it is necessary to resort to nickel and cobalt alloy matrixes [25]. This is consistent with the trend identified in the literature as, in recent works, Co-base alloys have become more prominent for the enhancement of surface properties of components working under high-temperature and severe conditions. Co-base alloys are known to have not only high abrasion and corrosion resistance but also to retain these properties at high temperatures, making them suitable for a wide range of applications [26]. However, if further strengthening or a major improvement of the wear resistance is required, a ceramic reinforcement (e.g. TiC, WC, SiC, etc.) can be embedded into the Co-base alloy matrix [27]. The addition of tungsten carbide ceramic particles to Stellite 6 coatings has been demonstrated to significantly enhance surface properties by increasing the resistance to wear and erosion, as stated in the literature by Bartkowski and Bartkowska [20]. Nonetheless, success stories in the manufacturing of such samples are still scarce in the literature. In most cases, cracking phenomenon, inhomogeneous dispersion of the reinforcement phase, or poor bonding between constituents are reported [28].

Another fundamental challenge that the manufacturing of MMCs by L-DED poses is the prediction of the properties of the matrix and the estimation of the normalized properties of the deposited material. Driven by this concern, microstructural and mechanical aspects of MMCs manufactured by L-DED have been investigated by some authors. Among the research on L-DED of MMCs published in the literature, the studies developed by Zhong et al. [29], Deschuytenner et al. [30], and Muvvala et al. [21] should be highlighted. Zhong et al. carried out an in-depth analysis of the microstructure generated when manufacturing tungsten carbide reinforced Stellite 6 through L-DED. They determined and characterised the main phases arising from the dilution of the reinforcing phase [29]. Deschuytenner et al., on the other hand, studied the hardness of MMCs consisting of a Ni-base alloy and tungsten carbide at different scales. They studied the evolution of the normalized hardness of the MMC, as well as the hardness achieved by the metal matrix [30]. Finally, Muvvala et al. studied the bonding produced between the ceramic particles and the metal matrix in MMCs consisting of Ni-base alloys and tungsten carbide. They concluded that the dissolution of the reinforcing phase played a significant role in the bonding type. They also monitored and correlated the melt pool lifetime with the thickness of the reaction layer generated around the reinforcing particles [21].

It is well known that the matrix properties and the bonding character between the constituents affect the final properties of the MMC [6,30]. Indeed, it has been reported that the enrichment of the metallic matrix strongly modifies its mechanical properties, which can be either enhanced or degraded [30]. Consequently, the mechanisms of dissolution of the reinforcement phase into the metal matrix need to be understood and controlled. Fuelled by this necessity, more recent works in the field have focused on investigating the metal-ceramic interaction during the L-DED of MMCs. Zhao et al. worked with wire-based L-DED and studied Ni-base alloy and tungsten carbide material systems in [31] and Fe-base alloy and tungsten carbide material systems in [32]. They identified different mechanisms leading to ceramic particle decomposition (namely, dissolution, diffusion, precipitation, and fragmentation of the ceramic particles). Additionally, the hardness of the matrix as well as the wear resistance of the coatings was investigated.

Nonetheless, most published research focuses on the microstructural and mechanical characterisation of MMCs, while no thorough investigation and discussion of the effect of the

process parameters and the thermal cycle of the manufacturing process is conducted. In fact, none of the previous authors obtained a correlation between the process parameters, microstructure, and the resulting properties of the coatings. Hence, the role of L-DED parameters on the formation of unexpected microstructural phases due to the particle–matrix interaction has been neglected and should still be under study. It is out of discussion that the L-DED parameters have a significant impact on the thermal cycle of the deposited material. Thus, process parameters affect the dissolution of the reinforcement particles and the mechanical properties of the metallic matrix and the composite. In order to facilitate the deployment of MMC coatings deposited by L-DED in the industry, it is essential to develop correlations between process parameters and mechanical properties of the deposited materials. To that end, in the present work, the influence of the process parameters on the metal-ceramic interaction in L-DED of MMCs, and the subsequent microstructural aspects and mechanical properties of the deposits are studied. Based on the existing literature, the novelty and contribution present in this research are to:

i. provide a systematic sensitivity and correlation study of process parameters in MMCs produced by L-DED and the thermal cycle of the manufacturing process.
ii. develop quantitative predictive models of key microstructural aspects and mechanical properties of MMCs produced by L-DED.
iii. present an in-depth microstructural and mechanical characterisation study of MMCs produced by L-DED by looking at the effect of key process parameters, namely thermal cycle, feedrate, and feedstock composition. The variation of the chemical composition of the matrix, the hardness of the matrix, and the hardness of the coating are analysed.

Another element of novelty is the combination of the statistical methods and material characterisation to corroborate the physical understanding of the governing phenomena in the L-DED of MMCs. This type of study was entirely lacking from existing literature.

2. Materials and methods

2.1. Materials

In the present work, commercial Co-base alloy (MetcoClad 6 from Oerlicon Metco) and tungsten carbide (MetcoClad 52001 from Oerlicon Metco) powders were employed as coating material. The Co-base alloy constitutes the metallic matrix, while the tungsten carbide particles act as discrete ceramic reinforcements. In Table 1 and Table 2, the granulometry and the composition of the powder feedstocks are detailed. The Stellite 6B (Hayness International) Co-base alloy was employed as the substrate to be coated. Five 6.35 × 50 × 50 mm^3 sized billets were employed, which ensured proper heat evacuation during processing and prevented substrate distortion. The composition of the substrate material is also shown in Table 2.

2.2. Empirical model

The objective of the present work is to establish an empirical model to correlate L-DED parameters and micro and macrostructural properties of the deposited MMC coatings. Experimental methodologies, in combination with the development of prediction tools, allow a better understanding of the extremely complex phenomena present in the L-DED of MMCs. According to Svetlizky et al. [36], this would help meet some critical industrial requirements concerning repair and coating applications.

Table 1
Granulometry of the L-DED powders employed [33,34].

Material	Maximum size (μm)	Minimum size (μm)
MetcoClad 6	106	45
MetcoClad 52001	106	45

The interaction between the ceramic and the metallic phase has a significant effect on the micro- and macro-properties of the deposited coatings. Therefore, the most significant factors ruling that phenomenon need to be determined to define the inputs of the model. In the case of tungsten carbide reinforced MMCs, the dissolution phenomenon is promoted by the low formation enthalpy of WC and the high temperatures inherent to every fusion-based manufacturing process. The thermal cycle of the manufacturing process and the composition of the material itself play a major role in ceramic-to-metal interaction [21]. Thus, in the case of the L-DED process, it is strongly influenced by the temperature and lifetime of the melt pool. It can be inferred that the properties of additively manufactured MMCs are given by the composition of the feedstock material and the thermal cycle of the L-DED process.

The thermal cycles in L-DED are characterised by having a high cooling rate and a morphology similar to that shown in Fig. 1. For the present work, the maximum temperature, T_{max}, and the time, Δt_T, during which the material is subject to a temperature higher than a certain threshold value, $T_{critical}$, are chosen as representative parameters for the thermal cycle.

The melting point of the metal matrix (i.e. 1260 °C [33]) was chosen as the threshold ($T_{critical}$) for the calculation of Δt_T. The decarburization reaction of the tungsten carbide is kinetically driven and, consequently, time- and temperature-dependent [37]. Thus, Δt_T will have a greater effect on the dissolution of the reinforcement phase into the metal matrix. Typically, the feedrate and the laser power control the thermal cycle in the L-DED processes. However, the predominant parameter influencing the time during which the material is subject to a temperature higher than the threshold set needs to be determined. To that end, a preliminary study of the influence of L-DED parameters on the thermal history of the L-DED process was necessary, named Stage 1 in Fig. 2. Afterwards, a statistical analysis based on the Design of Experiments (DOE) methodology was adopted to develop the empirical model to predict the micro- and macro-properties of MMC coatings, referred to as Stage 2 in Fig. 2.

2.2.1. Influence of the main L-DED parameters on the thermal cycle (Stage 1: Exploration)

A two-level full factorial two-way ANOVA analysis was designed to determine the factor having the most significant effect on the thermal cycle of the L-DED process. Two factors (FA and FB) were considered in Stage 1, namely, the laser power (FA) and the feedrate (FB). The representative parameters of the thermal cycle depicted in Fig. 1 were selected as response variables (Table 3).

The factor levels (Table 4) were established based on the typical window of parameters for the matrix material. The reference parameters resulted in defect-free and good-quality clads. Each test was carried out twice, thus, 8 specimens were fabricated in total.

In the exploration stage, the Co-base alloy (MetcoClad 6) with no reinforcement was used as feedstock material. The thermal cycle was measured at the central point of 20 mm-long single clads. To that end, a pyrometer was set in a static and off-axis position. The time vs temperature recorded by the pyrometer was further processed through Matlab R2022a software, to determine the response variables (T_{max}, $\Delta t_{1620\ °C}$) in each experiment.

Firstly, a main effect analysis was performed with averaged values of the repetitions. Pareto charts were built to provide a quali-

Table 2
Chemical composition of the L-DED powders and the substrate employed (in wt.%) [33–35].

Material	Co	Cr	W	Fe	Ni	Si	C	Mo
MetcoClad 6	Bal.	28.0	4.0	3.0	3.0	1.5	1.0	1.0
MetcoClad 52001	0.0	0.0	Bal.	0.19	0.0	0.0	4.03	0.0
Stellite 6B	Bal.	30.0	4.5	3.0	3.0	2.0	1.65	1.5

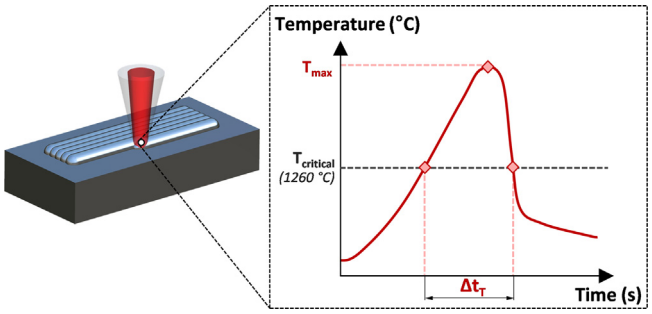

Fig. 1. Characteristic thermal cycle of the L-DED process.

tative evaluation of the significance of each factor in the responses. Eq. (1) shows the equation for the regression model of this analysis.

$$y_{ij} = \mu + \alpha_i D_A + \beta_i D_B + (\alpha\beta)_{ij} D_A \times D_B + u_{ij}; i,j = 1,2 \quad (1)$$

where D_A and D_B are the dichotomic variables of factors A and B, respectively. The main effect of the factors and the interaction were calculated as follows (Eq. (2)–(4)).

$$\alpha = \alpha_1 - \alpha_2 = 2\alpha_2 \quad (2)$$

$$\beta = \beta_2 - \beta_1 = 2\beta_2 \quad (3)$$

$$\alpha\beta = (\alpha\beta)_{22} - (\alpha\beta)_{12} = 2(\alpha\beta)_{22} \quad (4)$$

where α, β, and $\alpha\beta$ are the main effects of factor A, factor B, and interaction on the response variable, respectively.

Then, a two-way ANOVA study was carried out to quantitatively compare the p-value of the factors and the interaction, while accounting for the repeatability of tests. In this manner, the most significant L-DED parameter for the exploitation stage (Stage 2) was determined.

2.2.2. Empirical model to predict the micro- and macro-properties of MMC coatings manufactured by L-DED (Stage 2: Exploitation)

In the exploitation stage, Stage 2, an empirical model to predict the micro- and macro- properties was built. To that end, a statistical analysis based on DOE methodology was proposed, in particular the Response Surface Method (RSM) and Central Composite Design (CCD). The method was selected based on its robustness, low complexity, and data availability. The equation of the quadratic response surface model is given by Eq. (5).

$$Y = a_0 + \sum_{i=1}^{q} a_i x_i + \sum_{i=1}^{q} a_{ii} x_i^2 + \sum_{i=1}^{q} a_{ij} x_i x_j + \epsilon \quad (5)$$

where Y is the response variable, a_0 is the free term, a_i is the linear term, a_{ii} is the quadratic term, a_{ij} is the intersection term, x_i and x_j are the independent variables, q is the number of factors, and ε is the fitting error.

Two factors were chosen as input parameters of the model, namely, the tungsten carbide content of the feedstock and the feedrate. The latter was selected based on the results of the exploration stage, as the two-way ANOVA performed pointed at the feedrate as the dominant parameter concerning the $\Delta t_{1620\,°C}$. Three discrete levels were defined for each factor to account for the non-linearities of the studied phenomena (Table 5). Thus, the DOE comprised 9 runs (Table 6).

On the other hand, four responses were defined for the model (Fig. 2). Firstly, the hypothesis established in Stage 1 was confirmed. To that end, the thermal cycle of the material during the L-DED processing ($\Delta t_{1620\,°C}$) was studied. Then, the variation of the composition of the matrix was analysed through the W wt.% of the matrix. This parameter illustrates the extent of the metal-ceramic interaction. Lastly, the hardness of the matrix (HV0.3) and the overall hardness of the coating (HV30) were studied, at micro- and macro scales, respectively. In Table 7, the responses of the DOE are summarized.

The empirical model was fitted in the JMP Pro 16 software, and a backwards term elimination approach was used to systematically remove non-significant terms. A level of significance of 0.05 was established as the term elimination criteria, meaning that only those terms having a p-value lower than 0.05 were considered in the optimised model.

2.3. Coating production by L-DED

The TruLaser Cell 3000 laser-processing machine was employed to manufacture the specimens. A Yb:YAG disk laser of 3 kW maximum output power and 1030 nm wavelength was used. The diameter of the beam and the laser power were kept constant at 1.8 mm and 700 W, respectively. The powder feedstock was delivered through the GTV PF 2/2 powder feeder, whose two independently controlled hoppers allow for multi-material deposition. Lastly, the feedstock was injected into the melt pool by a discrete coaxial noz-

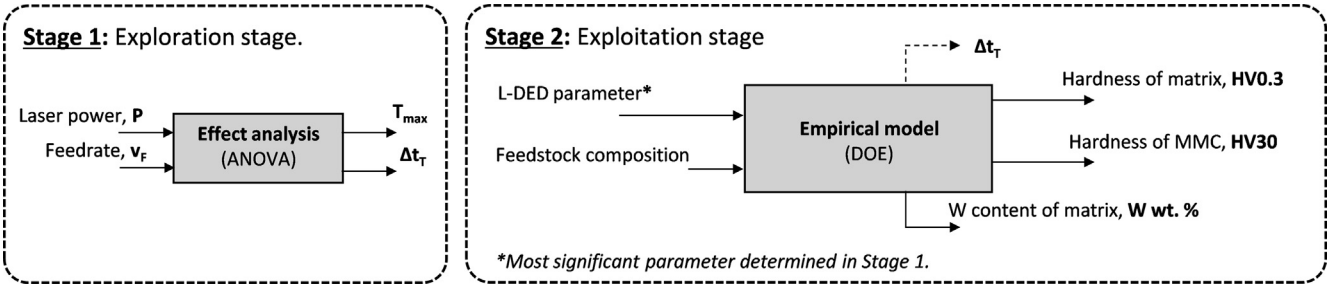

Fig. 2. Schematic illustration of the empirical study.

Table 3
Variables involved in the exploration experiments.

Factors	Responses
FA: Laser Power (P) FB: Feedrate (v_F)	R1: Maximum temperature reached during the L-DED process (T_{max}). R2: Time during which the temperature of the material is above 1260 °C ($\Delta t_{1620\ °C}$)

Table 4
Factors and levels in the ANOVA analysis.

Factors	Ref.	Level (-)	Level (+)
FA: Laser Power (P)	700 W	600 W	800 W
FB: Feedrate (v_F)	400 mm/min	300 mm/min	500 mm/min

Table 5
Summary of factors in the exploitation stage (S2).

Factors	Level −1.	Level 0	Level 1
Feedrate (v_F)	300 mm/min	400 mm/min	500 mm/min
Composition of feedstock (WC%)	10 %	25 %	40 %

Table 6
Specific build parameters of each run, feedrate (v_F) and tungsten carbide content (WC %).

Run	v_F (mm/min)	WC% (wt.%)
1	300	40
2	500	40
3	400	25
4	500	25
5	500	10
6	300	10
7	400	10
8	300	25
9	400	40

zle. Argon was used as the shielding gas and helium was used as the carrier gas, and they were set at a rate of 12 l/min and 4 l/min, respectively.

Two specimens were manufactured per run, whose composition and process parameters are detailed in (Table 6). The dimensions of the specimens were 17 × 17 × 1.2 mm^3. Four specimens were deposited in each billet, distributed per Fig. 3(a). Each specimen was constituted of two layers, which were deposited following a zig-zag strategy in X and Y directions, as shown in Fig. 3(b). During the deposition of the first layer, the temperature at the central point of the coating was measured employing a 2-colour IMPAC pyrometer (IGAR 12-LO LumaSense Technologies), which can measure temperatures between 550 °C and 2500 °C. A scheme of the experimental setup for the coating deposition is shown in Fig. 3(c).

2.4. Microstructural and mechanical characterisation

Firstly, a general metallographic inspection was carried out using a Leica DM2500 optical microscope. To that end, a cross-sectional sample of one of the deposited specimens was extracted. These samples were metallographically prepared and electrolytically etched with 10 % oxalic acid solution at 10 V and 1 A during 1–3 s.

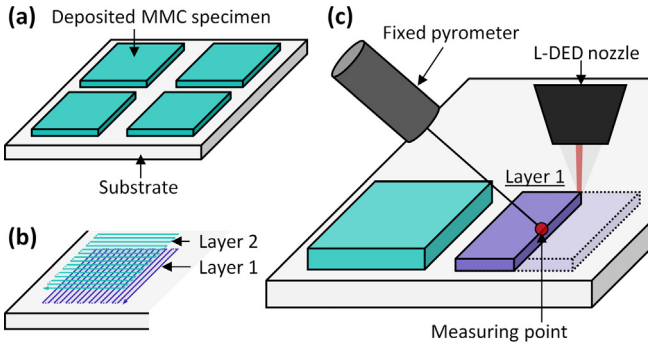

Fig. 3. (a) Distribution of the specimens in the substrate, (b) deposition strategy, and (c) detailed L-DED experimental setup for specimen preparation.

Secondly, a deeper evaluation of the microstructure and composition of the samples was carried out through scanning electron microscopy (SEM) and energy-dispersive X-ray spectroscopy (EDS). Two different systems were employed: (1) the Zeiss Ultra-Plus FE-SEM microscope with the Oxford Instruments X-MaxN 80 EDS, and (2) the Jeol JSM-IT500 SEM with an embedded EDS system. A cross-sectional sample of one of the deposited specimens was metallographically prepared for this purpose. For the compositional analysis of the metal matrix, four homogeneously distributed areas were systematically chosen along the coating (tungsten carbide particles were avoided during these measurements). The size of the studied regions was about 0.08 mm^2. In addition, point and line analyses were performed to determine the composition of the different microstructural phases present in the coatings. Moreover, the interaction between the WC particles and the metallic matrix was also inspected.

Thirdly, the hardness characterisation of the metal matrix was made by a Matsuzawa MMT-X7 micro Vickers hardness tester. The tests were performed in compliance with the ISO 6507–1:2018 standard [38]. The load of the test was selected based on the expected hardness and microstructure of the samples. Indentations should be big enough to comply with the standard but small enough to reflect only the influence of the matrix and not the reinforcement particles. Hence, the load was set at 2.94 N and the dwell time was 12 s. The indentations were made in metallographically prepared cross-sectional samples. One sample was investigated per run, which was extracted from the first specimen. 70 evenly distributed indentations were performed in each sample. The areas close to the substrate and the edges of the samples were excluded from the study and no indentations were performed in tungsten carbide particles or near them.

Lastly, the Duramin-A300 hardness testing system was used to macroscopically characterize the overall hardness of the surface of the specimens. To that end, the surface of the specimens was flattened, and its roughness was reduced by wire electro-discharge machining. The surface quality was further improved, and the affected region was eliminated by grinding with SiC papers. All

Table 7
Summary of responses in the exploitation stage (S2).

Response	Unit	Description	Measurement principle	No. Measurements per run
$\Delta t_{1620\ °C}$	s	Time during which the material is exposed to a temperature higher than 1620 °C.	Pyrometry	2
W%	wt. %	Tungsten content of the matrix.	EDS area	4
HV0.3	HV0.3	Hardness of the matrix.	Vickers micro-hardness	70
HV30	HV30	Hardness of the coating.	Vickers macro-hardness	15

tests were performed in accordance with the ISO 6507–2018 standard [38]. Similarly to the microscale characterisation, the load of the test was selected based on the hardness expected. The load should be high enough for the test to account for the matrix and reinforcement particle contributions. At the same time, the influence of the substrate should be avoided. Consequently, for the macro characterisation, the load was set at 294.2 N and the dwell time was 12 s. One sample was investigated per run, which corresponded to the second specimen. In each sample, 15 homogeneously distributed indentations were made.

3. Results

3.1. Influence of the main L-DED parameters on the thermal cycle (Stage 1: Exploration)

In the exploration stage of the present study, the most significant L-DED parameter for the exploitation stage, Stage 2, was determined. To that end, a full factorial two-level and two-way ANOVA study was performed with the factors and responses depicted in Table 3. For each response, an independent analysis was carried out. Table 8 shows the results of each specimen fabrication corresponding to R1 and R2.

Based on average values, a main effect analysis of each response was carried out and it was represented by Pareto charts (Fig. 4). The main effects of the laser power, the feedrate, and the interaction are given by α, β, and αβ, respectively. As expected, the laser power is the most significant factor concerning the maximum temperature of the L-DED process, while the feedrate is the main factor affecting the time during which the material is above 1260 °C.

The variance of the phenomena was accounted for, and the repeatability of the experiments was considered, in the two-way ANOVA analysis. The summary of this analysis is shown in Table 9. A substantially lower p-value was obtained for FA in the R1, and for FB in the R2, which is in good agreement with the main effect analysis of the averaged values previously shown.

Based on the statistical analysis performed in the exploration stage, the influence of the main L-DED parameters on the thermal cycle of specimens deposited by means of L-DED was better understood. The target parameter, $\Delta t_{1620\ °C}$, is mainly controlled by the feedrate. Consequently, only the feedrate was considered in the exploitation stage.

3.2. Empirical model to predict the micro- and macro-properties of MMC coatings manufactured by L-DED (Stage 2: Exploitation)

In the exploitation stage (Stage 2) statistical models describing the micro- and macro-properties of MMC coatings were fitted. This research focuses on developing regression models of the thermal cycle of the L-DED process, the composition of the matrix, the hardness of the matrix, and the hardness of the coating. Additionally, the correlations were supported by an in-depth analysis of the microstructure and the physical phenomena governing the interaction between the matrix and the ceramic particles.

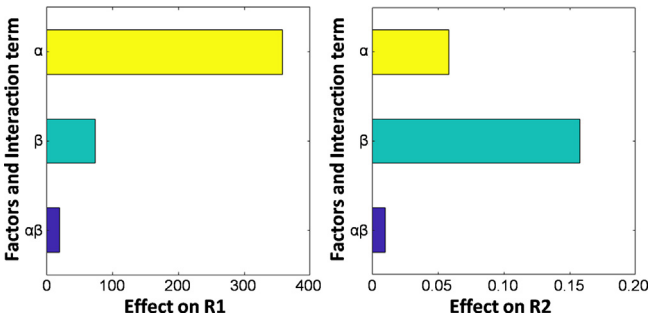

Fig. 4. Pareto charts of the main effects of R1 (T_{max}) and R2 ($\Delta t_{1620\ °C}$).

Table 9
Summary of the two-way ANOVA study.

Factor	P-value	
	R1: T_{max} (°C)	R2: $\Delta t_{1620\ °C}$
FA: P (W)	4.74E-8	1.04E-4
FB: v_F (mm/min)	2.56E-5	1.98E-6
FAB: Interaction	4.26E-3	5.36E-2

In Table 10, a summary of the performed DOE is shown. Average values of all four responses together with the standard deviation are presented.

3.2.1. Influence of the feedrate on the thermal cycle, $\Delta t_{1620\ °C}$

The first model aims to further understand the influence of the feedrate on the thermal cycle of L-DED. In this manner, the hypothesis established in the exploration stage was validated.

After applying the backwards term elimination, only the linear and the quadratic terms of the feedrate remain significant. Consequently, the tungsten carbide content of the feedstock material lacks enough statistical relevance for this response, and it can be neglected. In Table 11, the variance analysis of the RSM model is shown. The low p-value obtained for the fitting demonstrates the statistical significance of the model.

The equation of the quadratic response surface model is given by Eq. (6).

$$\Delta t_{1260^{\circ}C}(s) = 1.553 - 4.160 \cdot 10^{-3} \cdot v_F + 3.500 \cdot 10^{-6} \cdot v_F^2 \quad (6)$$

A multiple correlation coefficient (R^2) of 99.53 % and an adjusted R^2 of 99.37 % were achieved in the RSM model, while the root-mean square deviation (RMSE) obtained was as low as 0.0095. Thus, the predicted and experimental values are in good accordance. The results obtained in the exploitation stage support the exploration analysis. Consequently, the hypothesis established in Stage 1 was validated.

The correlation between the response ($\Delta t_{1620\ °C}$) and the feedrate is represented in Fig. 5(a). The actual vs predicted plot of the fitting is shown in Fig. 5(b), where good accordance between the predicted values and the experimental values is observed. In Fig. 5(c) the relative error of each specimen is plotted, the maximum relative error of the model being approximately 3 %.

Table 8
Experimental results of the exploration stage.

P (W)	v_F (mm/min)	$R1_1$ (°C)	$R1_2$ (°C)	$R2_1$ (s)	$R2_2$ (s)
600	300	1611.6	1606.9	0.360	0.351
800	300	1983.6	1989.5	0.424	0.424
600	500	1557.4	1552.6	0.202	0.214
800	500	1887.8	1897.9	0.255	0.257

Table 10
Summary of the DOE results.

Run	Factors		Responses			
	v_F (mm/min)	WC% (wt. %)	$\Delta t_{1620\ ^\circ C}$ (s)	W% (wt. %)	HV0.3	HV30
1	300	40	0.633 ± 0.024	36.6 ± 0.7	859 ± 46	937 ± 26
2	500	40	0.358 ± 0.011	31.8 ± 1.4	777 ± 38	920 ± 65
3	400	25	0.459 ± 0.000	24.2 ± 0.7	740 ± 33	775 ± 40
4	500	25	0.343 ± 0.006	22.1 ± 1.5	712 ± 50	772 ± 37
5	500	10	0.344 ± 0.007	12.4 ± 0.8	573 ± 30	565 ± 13
6	300	10	0.611 ± 0.011	11.0 ± 0.3	553 ± 18	522 ± 18
7	400	10	0.445 ± 0.017	12.0 ± 0.3	570 ± 24	541 ± 18
8	300	25	0.617 ± 0.033	25.2 ± 0.5	891 ± 70	788 ± 26
9	400	40	0.444 ± 0.009	33.7 ± 2.5	887 ± 58	872 ± 64

Table 11
Variance analysis of the RSM fitting for $\Delta t_{1620\ ^\circ C}$.

Source	Df	SS	MS	F-ratio	p-value
Model	2	0.113426	0.056712	630.144	1.060E-7
v_F	1	0.110976	0.110976	1233.067	3.555E-8
v_F^2	1	0.002450	0.002450	27.222	1.981e-3
Error	6	0.000540	0.000090		
C. Total	8	0.113966			

where Df are the degrees of freedom, SS is the sum of deviation squared, and MS is the mean sum of deviations squared.

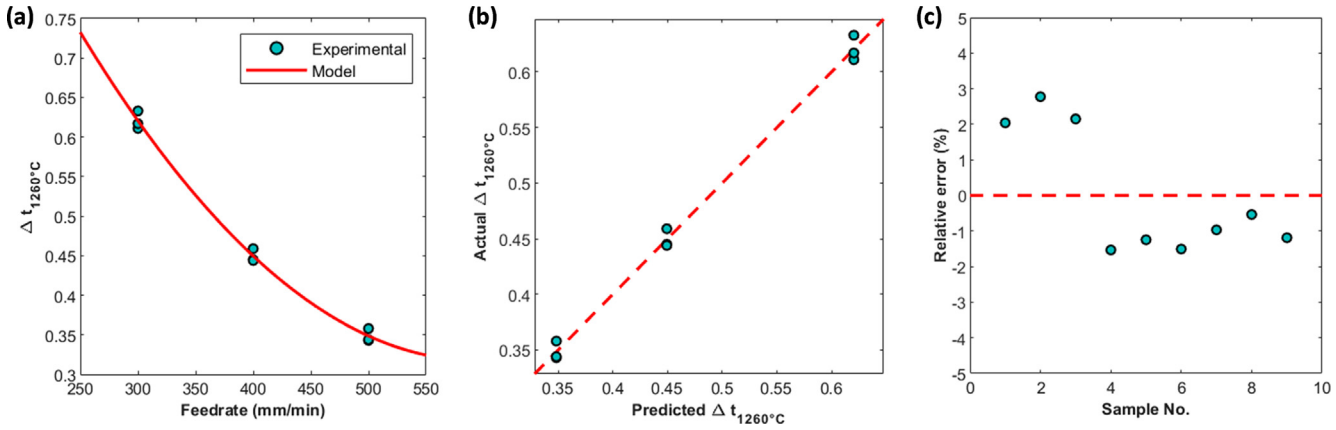

Fig. 5. (a) Comparison between the RSM model for $\Delta t_{1620\ ^\circ C}$ and the experimental results; (b) actual vs predicted plot, and (c) relative error of the model as compared to the experimental values.

3.2.2. Influence of the feedrate and the composition of the feedstock on the composition of the metal matrix, W%

The second model of the present study aims at predicting the average composition of the metallic matrix. This composition will be modified as a result of the interaction between the metal matrix and the discrete ceramic particles during the high-temperature processing. To that end, four discrete EDS area analyses were performed on each specimen. In Fig. 6, one of the areas employed for the compositional analysis in specimen 7 is shown as an example.

According to the results obtained from the backwards term elimination, only the linear terms of both factors and the interaction term have enough statistical significance on the average composition of the metal matrix. Thus, the other terms of the original quadratic RSM were excluded from the model fitting. In Table 12, the variance analysis of the correlation is shown. The low p-value of the model suggests that the model has high statistical relevance. Thus, the influence of the factors and the interaction on the response variable was confirmed.

The equation of the linear RSM is given by Eq. (7).

$$W\% = -1.264 + 1.486 \cdot 10^{-2} \cdot v_F + 1.153 \cdot WC\% - 1.028 \cdot 10^{-3} \cdot v_F \cdot WC\% \quad (7)$$

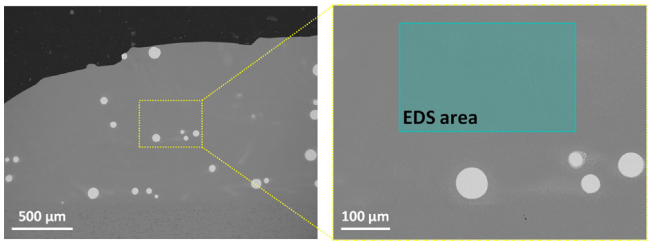

Fig. 6. Example of the area selected for the compositional analysis of the matrix. *(Specimen 7, area 1 of 4).*

In this fitting, an R^2 of 99.62 %, an adjusted R^2 of 99.40 %, and an RSME of 0.07493 were attained, which suggests good adequacy between the predicted and the empirical values.

A contour plot of the W% of the matrix as a function of the WC% of the feedstock and the feedrate is shown in Fig. 7(a). The higher density of isoW% lines in the vertical direction suggests that the WC% of the feedstock is the dominant factor in the model. Nonetheless, in specimens with higher values of WC%, the influ-

Table 12
Variance analysis of the RSM fitting for W%.

Source	Df	SS	MS	F-ratio	p-value
Model	3	759.93472	253.312	442.5715	1.754e-7
v_F	1	7.05250	7.05250	12.3217	1.71e-2
WC%	1	743.37270	743.37270	1293.778	3.097e-7
v_F·WC%	1	9.50951	9.50951	16.6145	9.577e-3
Error	5	2.86182	0.572		
C. Total	8	762.79654			

ence of the v_F becomes more significant. In specimens with lower WC%, the effect of the v_F is residual. This evidences the significance of the interaction between the factors. The actual vs predicted plot of the W% fitting (Fig. 7(b)) shows that the experimental and the predicted values are in good agreement, and the maximum relative error obtained is around 4.3 % (Fig. 7(c)).

3.2.3. Influence of the feedrate and the composition of the feedstock on the hardness of the metal matrix, HV0.3

The varying compositions in the studied specimens will presumably have an impact on the mechanical properties of the matrix, especially on the hardness. Therefore, the third model of the present study intends to capture this phenomenon by predicting the hardness of the matrix.

The backwards term elimination procedure showed that the v_F has little effect on the overall model, leaving the WC% as the only statistically relevant term. Nonetheless, the feedrate was expected to have an impact on the hardness of the matrix. Consequently, the v_F was taken into consideration for the model fitting. Additionally, the quadratic term of the WC% was also added to the model in pursuit of statistical coherence. In fact, this term had a lower p-value as compared to the v_F. The variance analysis for the HV0.3 model is shown in Table 13. The p-value of this model is low, presumably indicating a good statistical significance of the model.

The equation of the RSM is given by Eq. (8).

$$HV0.3 = 495.721 - 4.033 \cdot 10^{-1} \cdot v_F + 2.656 \cdot 10^{1} \cdot WC\% - 3.474 \cdot 10^{-1} \cdot WC\%^2 \quad (8)$$

In this fitting, an R^2 of 89.70 %, an adjusted R^2 of 83.51 %, and an RSME of 55.8908 were attained. These values indicate that the correlation between the predicted and empirical values is good, even if it is not as good as that obtained in the previous models.

Fig. 8(a) illustrates the correlation between the hardness of the matrix, the feedrate, and the WC% fed. The composition of the feedstock has the most significant impact on the response studied. The contour plot could mislead one into assuming that the feedrate has a significant impact on the response. Nonetheless, this hypothesis was rendered invalid by examining the actual vs predicted plot (Fig. 8(b)). If the specimens are classified according to the WC% and each group is looked at independently, only the specimens with 25 %WC follow the trend of the RSM well. 10 %WC specimens not only do not follow the trend of the RSM model but the opposite trend is observed. Consequently, while the feedrate does have an active effect on the hardness, the model fails to predict such a phenomenon. Hence, the high p-value of this factor. Lastly, the relative errors obtained were higher in this case, as they reached 10 % in certain samples (Fig. 8(c)).

3.2.4. Influence of the feedrate and the composition of the feedstock on the surface hardness of the coating, HV30

The fourth predictive model relies on macroscopic hardness testing for data acquisition. The scale of the measurements is suitable for the characterisation of the hardness of the material system, as the contribution of both the matrix and the reinforcement particles is accounted for.

The linear and quadratic terms of the WC% were the only terms that possessed a p-value lower than 0.05. Thus, based on the backwards term elimination, all other terms should be eliminated from the fitting model. Nonetheless, the interaction between the two factors was included in the model. Even if the hardness of the composite is most affected by the volumetric fraction of each constituent, the feedrate has a different effect on the response depending on the WC% of the feedstock. The dominant strengthening mechanism is not the same throughout the experimental domain studied. The interaction term illustrates the different strengthening mechanisms. Hence, from a scientific perspective, it was interesting to include this term. The variance analysis for the HV30 model is shown in Table 14. The p-value of this model is quite low, which confirms its statistical significance.

The equation of the RSM is given by Eq. (9).

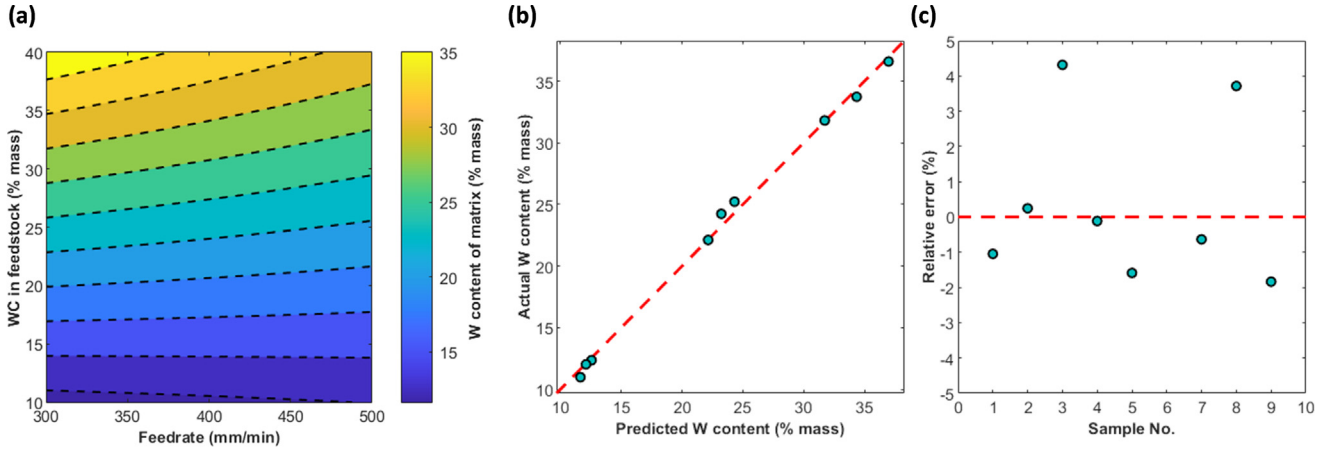

Fig. 7. (a) Contour plot of the RSM model for the W% in the matrix; (b) actual vs predicted plot; and (c) relative error of the model as compared to the experimental values.

Table 13
Variance analysis of the RSM fitting for HV0.3.

Source	Df	SS	MS	F-ratio	p-value
Model	3	135973.26	45324.4	14.5095	0.0067
v_F	1	9757.44	9757.44	3.1236	0.1374
WC%	1	113993.68	113993.68	36.4922	0.0018
WC%^{2}	1	12222.14	12222.14	3.9126	0.1048
Error	5	15618.89	3123.8		
C. Total	8	151592.15			

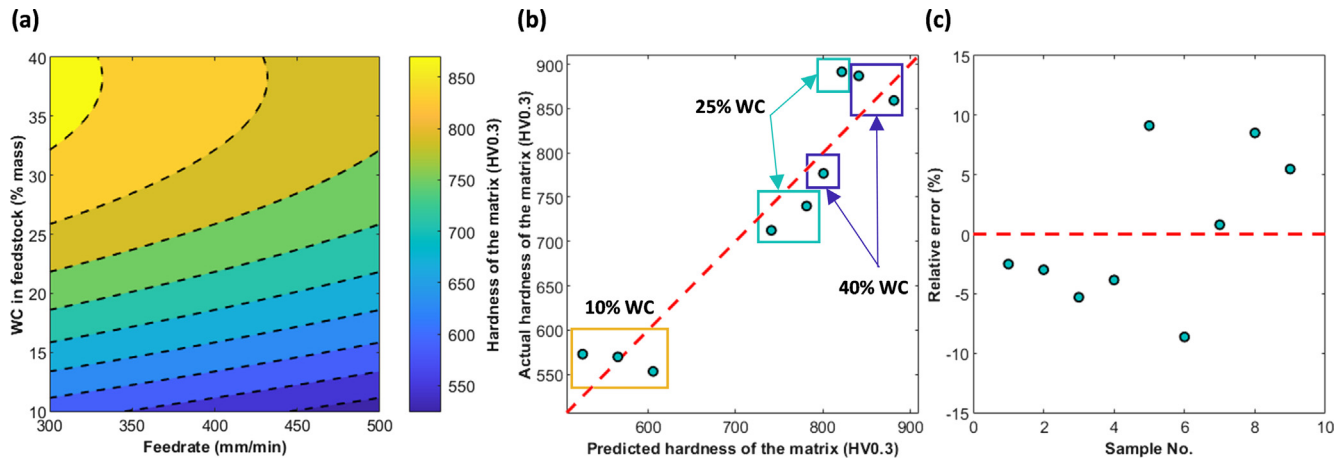

Fig. 8. (a) Contour plot of the RSM model for the hardness of the matrix, HV0.3; (b) actual vs predicted plot; and (c) relative error of the model as compared to the experimental values.

$$HV30 = 227.99 + 2.513 \cdot 10^{-1} \cdot v_F + 2.775 \cdot 10^{1} \cdot WC\% - 2.23 \cdot 10^{-1} \cdot WC\%^2 - 1.005 \cdot 10^{-2} \cdot v_F \cdot WC\% \quad (9)$$

In this fitting, an R^2 of 98.86 %, an adjusted R^2 of 98.18 %, and an RSME of 21.9048 were attained. These values indicate that the correlation between the predicted and empirical values is excellent. Thus, the ability of the model to represent the desired phenomena was confirmed.

The RSM model is represented in Fig. 9(a). The effect of the interaction is clearly shown, and different trends of the response are observed depending on the region of the experimental domain. The actual vs predicted plot (Fig. 9(b)) shows that the model follows the experimental values closely. Lastly, the maximum relative error is about 4 % (Fig. 9(c)).

4. Discussion

4.1. Influence of the feedrate on the thermal cycle, $\Delta t_{1620\ °C}$

The temperatures recorded by the pyrometer during the deposition of each specimen are shown in Fig. 10. As suggested by the RSM model (Fig. 5(a)), the thermal cycle of the L-DED process is mainly influenced by the feedrate. Higher feedrates lead to higher cooling rates and lower $\Delta t_{1620\ °C}$, which is expected to limit the interaction between the ceramic and the metallic phase. Oppositely, lower feedrates promote the decomposition of the ceramic phase. Thus, the composition and the mechanical properties of the matrix will be affected to a greater extent.

4.2. Influence of the feedrate and the composition of the feedstock on the composition of the metal matrix, W%

The statistical analysis performed revealed the variability of the interaction between the metal matrix and the discrete ceramic particles with regard to the L-DED parameters and the composition of the feedstock (Fig. 7(a)). The thermal nature of the L-DED process gives rise to phenomena as complex as the diffusion between the matrix and the reinforcement phase, or the decomposition and precipitation of the WC particles. The high temperatures inherent to the manufacturing process foster the decomposition of the WC particles. The subsequent reaction with the metal matrix through different mechanisms results in a reaction layer around the discrete ceramic particles. Examples of the different interaction mechanisms present in the investigated samples are shown in Fig. 11. In some cases, the precipitation of W-rich phases is the dominant phenomenon (Fig. 11(a)). During the solidification process, the interface between the particle and the matrix is the preferent site for the nucleation of W-rich dendrites. In other cases, the

Table 14
Variance analysis of the RSM fitting for HV30.

Source	Df	SS	MS	F-ratio	p-value
Model	3	208166.46	59388.8	144.6148	2.811E-5
WC%	1	201901.40	201901.40	420.7874	0.00001
v_F·WC%	1	5355.44	5355.44	11.1614	0.22701
WC%^{2}	1	909.63	909.63	1.8958	0.02053
Error	5	2399.09	479.8		
C. Total	8	210565.55			

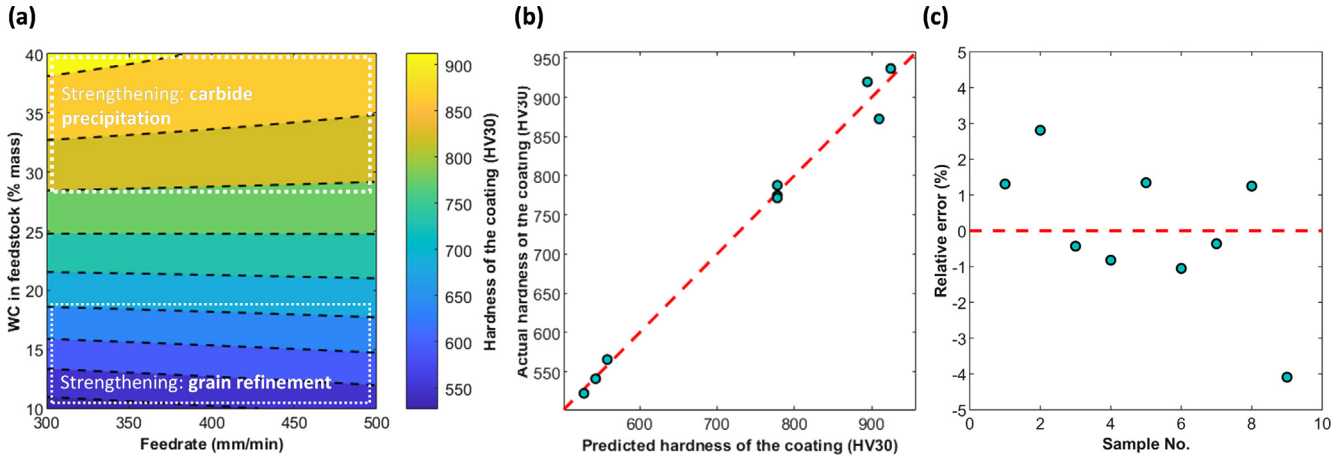

Fig. 9. (a) Contour plot of the RSM model for the surface hardness of the coating, HV30; (b) actual vs predicted plot; and (c) relative error of the model as compared to the experimental values.

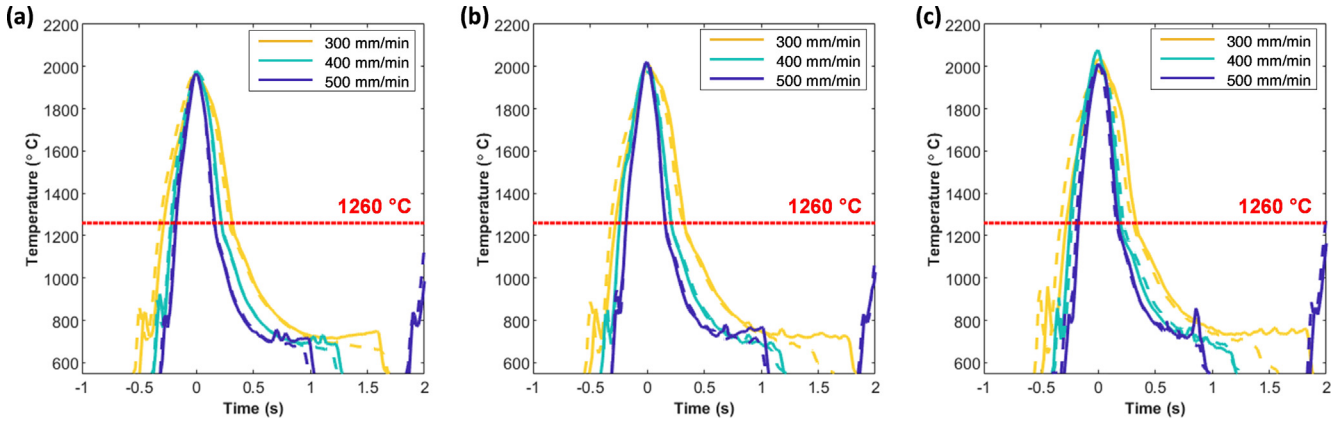

Fig. 10. Thermal cycles recorded by the pyrometer during the L-DED process. Specimens with: (a) 10 %WC, (b) 25 %WC, and (c) 40 %WC (Continuous and dashed lines correspond to the first and second specimens, respectively). Note that the origin of the X-axis (time) is set at the temperature peak of the thermal cycle. In this manner, the variation of the thermal cycle with the federate can be better understood.

nucleation of dendrites is inhibited, and diffusion is found to be the dominant interaction mechanism (Fig. 11(b)). However, typically a combination of both mechanisms is present (Fig. 11(c)).

Due to this interaction, unexpected microstructural phases are created in the surroundings of the ceramic particles. The light phases in Fig. 12 correspond to tungsten rich phases, which form during the solidification and are a result of the diffusion and precipitation of the ceramic phase. The EDS elemental analysis showed that this phase contains roughly 65 % of tungsten in weight. They have been identified as W-rich complex carbides in the literature [31,32]. When a high WC% feedstock is employed (Fig. 12(a)), these W-rich phases are dispersed all over the matrix (Fig. 13). Consequently, the overall tungsten content of the matrix increases, as suggested by the model. Presumably, these dispersed tungsten phases will raise the hardness of the matrix material. However, when lower WC% feedstock was employed (Fig. 12(b)), the W-rich phases were found mostly in the surroundings of the ceramic particles.

The EDS maps in Fig. 14 clearly illustrate the extent of the interaction between the discrete particles and the matrix. Fig. 14(a) and (b) correspond to low and high WC% in the feedstock, respectively. The matrix of specimen 9 was much more affected and its composition altered significantly. The tungsten map revealed the presence of tungsten-rich phases in the matrix. The matrix of

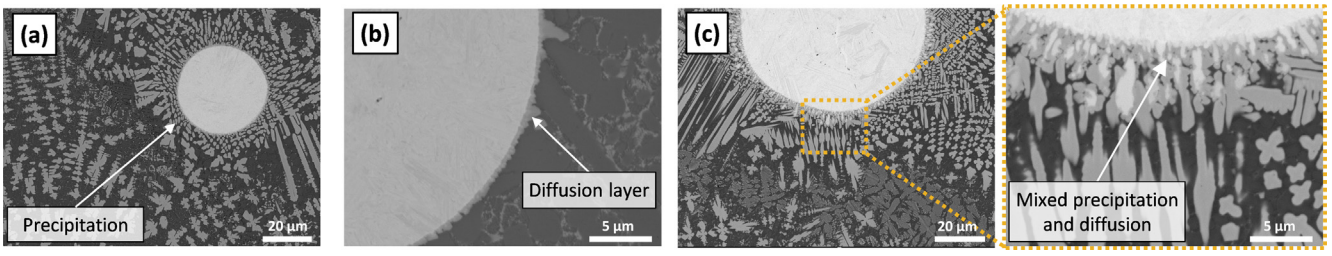

Fig. 11. Interaction mechanisms between the discrete ceramic particles and the metal matrix. (a) Specimen 1: 40 % WC and 300 mm/min, (b) specimen 4: 25 % WC and 500 mm/min, and (c) specimen 9: 40 % WC and 40 mm/min.

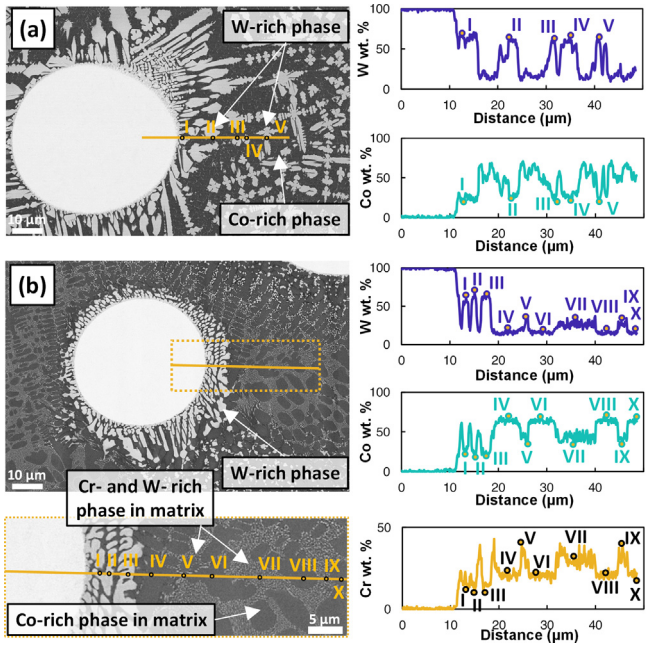

Fig. 12. EDS line analysis of the microstructural phases surrounding ceramic particles: (a) specimen 9: 40 %WC and 400 mm/min and (b) specimen 8: 25 %WC and 300 mm/min.

specimen 7, however, was only affected around the ceramic particle. A reaction layer with higher tungsten content was identified, but cobalt and chrome phases remained dominant in the matrix. The thermal cycle of both fabrications was similar, as they were both manufactured at 400 mm/min. However, due to the higher amount of WC particles in the feedstock, more W was readily available to react with the matrix in specimen 9.

The decomposition of the ceramic phase and its interaction with the metal matrix has a strong influence on the microstructural aspects of the matrix of MMC coatings. Not only when different feedstock compositions are used, but also when different L-DED parameters are employed. For instance, when the specimens manufactured at 500 mm/min and 300 mm/min are compared (Fig. 15 (a) and (b)), a higher volumetric fraction of the interdendritic phase is observed in the latter. The EDS line analysis revealed that this phase has higher Cr and W contents (points V, VII, and IX in Fig. 12(b)), as compared to the Co-rich dendrites (points IV, VI, VIII, and X in Fig. 12(b)). The interdendritic phase is composed of the eutectic phase and Co, W, and Cr carbides [39]. The lower cooling rates inherent to the slower processing of the material allowed the ceramic and metallic phases to interact for a longer time. Thus, a higher amount of tungsten carbide was decomposed, which promoted the formation of the interdendritic phase. This phenomenon was captured by the RSM model, which showed a direct correlation between the W content of the matrix and the feedrate, especially when feedstocks containing over 20 %-25 % WC were employed (Fig. 7(a)). Conversely, when more tungsten carbide was introduced into the feedstock material, the tungsten originally belonging to the ceramic phase was not located in the interdendritic phase solely. W-rich complex carbides (Fig. 15(d)) with different morphologies (faceted or herringbone, for instance), were dispersed in the matrix of the coating.

4.3. Influence of the feedrate and the composition of the feedstock on the hardness of the metal matrix, HV0.3

The high dispersion observed in the empirical data had an impact on the lack of fit of the RSM model of the hardness of the matrix (Table 10). This variability was ascribed to two aspects mainly:

(1) Heterogeneity of the microstructure and the mechanical properties at the microscopic scale of L-DED coatings.
(2) Uneven distribution of the tungsten carbide particles throughout the specimens.

The L-DED process is based on the subsequent deposition of clads and layers to build a part or, in this case, to coat a part. The resolution of the process changes with the clad size, both in terms of geometry and property homogeneity. When a clad is deposited, a region of the previous clad is thermally affected. Thus, the microstructure of the heat-affected zone is modified, and so are its mechanical properties. The reheating and remelting principle applies to the deposition of subsequent layers too. Consequently, a variation in the hardness of L-DED deposited specimens is expected, especially when microscopic testing methods are employed. In Fig. 16, the impact of the deposition of the second layer is observed. The carbides in the interdendritic phase tend to coarsen due to the reheating cycles. Consequently, the carbides in the as-deposited region (lower section of the picture) are finer as compared to those found in the heat-affected zone. This phenomenon has an impact on the hardness of the material and justifies the high dispersion observed in microhardness measurements (Table 10).

On the other hand, the uneven dispersion of the discrete tungsten carbide particles will add up to the hardness variation of the specimens. The tungsten carbide particles are randomly distributed during the L-DED process, and their location cannot be controlled. Their distribution depends mostly on the speed of solidification, the melt pool dynamics, and the behaviour of the nozzle. Thus, the matrix will be unevenly affected by the particle–matrix interaction. In Fig. 17, the microstructural heterogeneity due to the uneven particle–matrix interaction of specimen 9 is observed. Additionally, the EDS map shows a high variation of the W% content in the matrix, which is partially responsible for the dispersion observed in the hardness measurements.

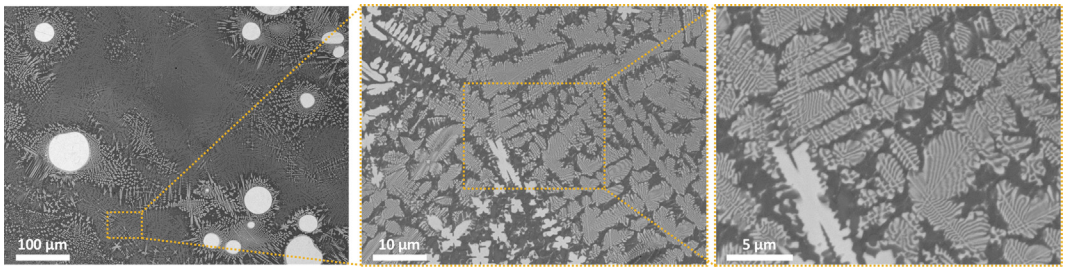

Fig. 13. W-rich phases dispersed all over the matrix in specimen 9 (40 %WC and 400 mm/min).

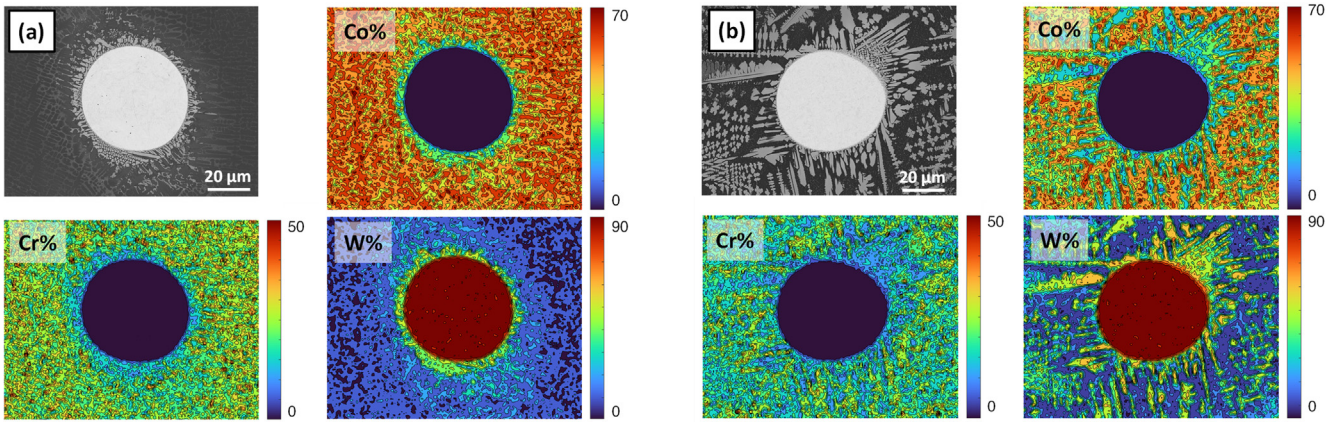

Fig. 14. EDS maps of the interaction between the ceramic and metal phases in (a) specimen 7: 10 %WC and 400 mm/min and (b) specimen 9: 40 %WC and 400 mm/min.

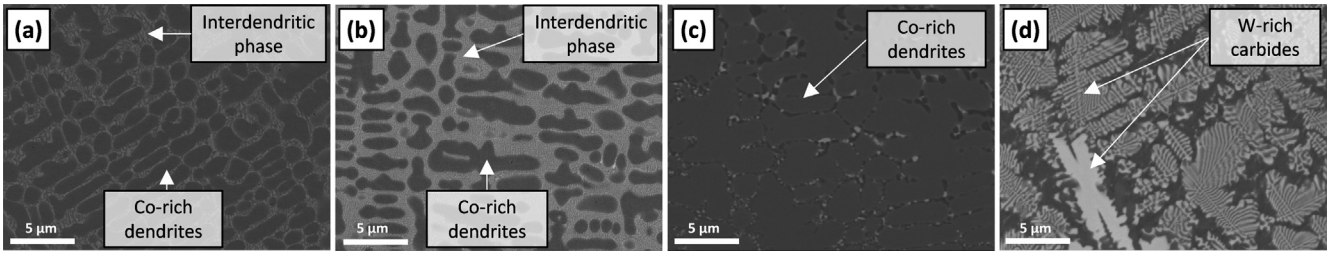

Fig. 15. SEM images of the matrix of the specimens. (a) Specimen 4: 25 %WC and 500 mm/min, (b) Specimen 8: 25 %WC and 300 mm/min, (c) Specimen 7: 10 %WC and 400 mm/min and (d) Specimen 9: 40 %WC and 400 mm/min.

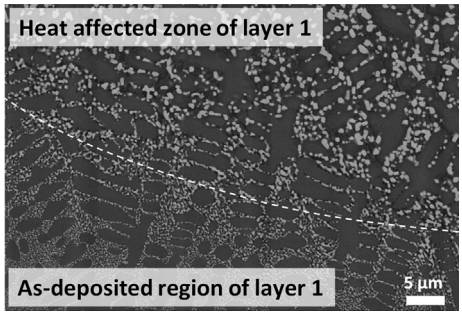

Fig. 16. Effect of the deposition of subsequent layers in the microstructure of the matrix. Specimen 8: 25 %WC and 300 mm/min.

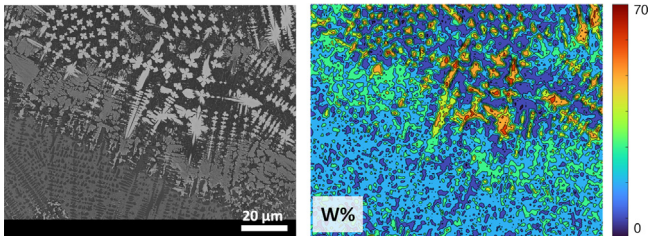

Fig. 17. Heterogeneous microstructure of the matrix due to the heterogeneous particle distribution and, consequently, uneven matrix-particle interaction. Specimen 9: 40 %WC and 400 mm/min.

The lack of microstructural homogeneity at the microscopic scale of the response variable limits the accuracy of the RSM fitting. Qualitative trends could be extracted, and the hardness of the coatings could be roughly estimated. However, macroscopic measuring methods are a better data source.

4.4. Influence of the feedrate and the composition of the feedstock on the surface hardness of the coating, HV30

The RSM model revealed different trends of the HV30 depending on the specific region of the studied experimental domain (Fig. 9(a)). The interaction between the factors of the model is key to understanding the different strengthening mechanisms and their role throughout the experimental domain. In the specimens with higher tungsten carbide content, lower feedrates increased the surface hardness. In this area, the dominant strengthening mechanism was carbide precipitation. This is accomplished through solid-solution alloying of carbide forming elements, namely, tungsten. The solid-solution of such elements in combination with carbon, promoted the formation and dispersion of complex carbides, which led to an increase in the hardness of Co-base alloys [40]. The decomposition of the tungsten carbide particles is thermally activated. Lower feedrates resulted in a greater amount of tungsten migrating into the matrix. Therefore, the precipitation of carbides and hard phases was fostered (Fig. 15(d)).

However, if the WC% decreased, the trend shifted. Higher feedrates led to higher surface hardness. In this area, grain refinement was responsible for the differences in hardness. Highly refined microstructures result in higher hardness [41]. Higher thermal gradients were attained when higher feedrates were employed. Hence, a finer microstructure was observed in the specimen manufactured at 500 mm/min, as opposed to the specimen manufactured at 300 mm/min (Fig. 18).

Based on the above discussion, in regions with intermediate WC %, lower feedrates could potentially result in a hardening effect due to the increase of W% of the matrix, by solid-solution and carbide precipitation. However, the increase of the grain size derived from

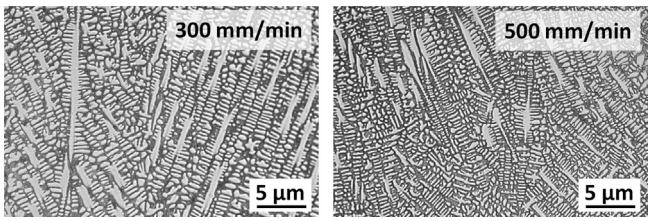

Fig. 18. Grain size comparison. (a) Specimen 6 (10 %WC and 300 mm/min) and (b) Specimen 5 (10 %WC and 500 mm/min).

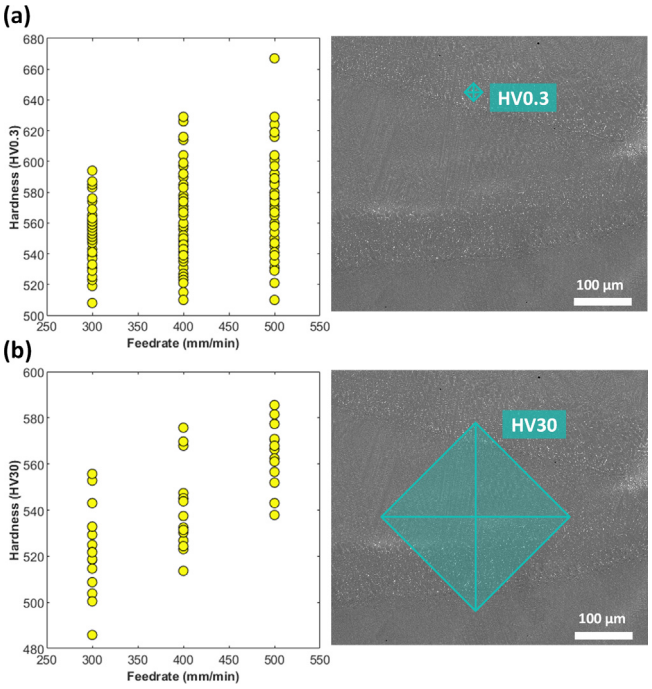

Fig. 19. Hardness characterisation of the 10 %WC specimens at (a) microscopic and (b) macroscopic scales.

a lower thermal gradient counteracts this effect. Hence, a negligible variation of the hardness is observed even when modifying the process parameters. This effect is clearly illustrated in runs 3 and 4 of Table 10. At 25 % WC, when reducing the feedrate from 500 mm/min to 400 mm/min, the W% of the matrix varies accordingly, from 22.1 ± 1.5 to 24.2 ± 0.7. Nonetheless, the hardness of the composite remains similar, at 772 ± 50 HV30 and 740 ± 33 HV30, respectively.

A comparison between the hardness characterisation methods in 10 %WC specimens is shown in Fig. 19. A higher dispersion was found when microscopic test methods (a) were used. In the scatter plot a trend can be guessed, which suggests that higher feedrates will result in harder matrixes. However, the high dispersion of the experimental data hides this effect. This method is only valid to characterise the matrix, as the influence of the reinforcement phase in the test is avoided. Macroscopic test methods result in lower dispersion, although a significant variability of the hardness is still present. Considering the scale of the hardness test, the measurements will still reflect material heterogeneities owing to uneven particle distribution and varying thermal histories. Nonetheless, given the lower resolution of the characterisation method, clearer trends than in HV0.3 are observed.

5. Conclusions

In the present work, the microstructural and macrostructural aspects of MMC coatings deposited by L-DED were analysed. To that end, an experimental approach supported by statistical methods was adopted. Firstly, the L-DED parameter having the most significant effect on the thermal cycle of the L-DED process was identified. Then, four variables were modelled through a DOE-based methodology. Namely, the thermal cycle of the L-DED process, the composition of the matrix, the hardness of the matrix, and the surface hardness of the coating were analysed. More importantly, the physics behind these models were studied and understood.

The main global contributions of the research are as follows:

(1) The interaction between the ceramic particles and the matrix has a major role in the microscopic and macroscopic properties of MMCs.
(2) The metal-ceramic interaction is thermally driven. Therefore, the high-processing temperatures of L-DED affect the properties of the material. Controlling the thermal cycle of the deposition process is key to tailoring the microstructure of the matrix.
(3) The time during which the material is exposed to a temperature higher than the melting point of the matrix ($\Delta t_{1260\ ^\circ C}$) has a strong impact on the interaction between the matrix and the reinforcement phase. The composition of the matrix can be targeted by controlling this parameter.
(4) The $\Delta t_{1260\ ^\circ C}$ depends mainly on the feedrate. Consequently, the composition of the matrix can be controlled by modifying the feedrate.
(5) In terms of the hardness of the matrix, testing at the microscopic scale (HV0.3) was found to be inadequate. The high heterogeneity of the specimens affects the quality of the data, as the resolution of the testing method captures this heterogeneity. Macroscopic characterisation methods (HV30) are found to perform better. However, the application of each method should be kept in mind. Macroscopic methods are only valid for the characterisation of the composite, meaning that the contributions of the matrix and the reinforcement phase are accounted for.

The composition and microstructural aspects of the matrix are influenced by both L-DED parameters, and the composition of the feedstock employed:

(1) When a high WC% is introduced into the feedstock (40 % WC), the effect of the feedrate on the composition of the matrix is significant. Lower feedrates result in longer interaction times. Longer exposition to high temperatures promotes the reaction of the ceramic and metallic phase. As a result, W-rich phases are dispersed all over the metal matrix.
(2) When feedstocks with intermediate WC content are employed (25 % WC), the feedrate affects the microstructure differently. A longer exposition to high temperatures also increases the W% of the matrix. However, in this case, the formation of the W-rich interdendritic phase is fostered. Consequently, in the specimen manufactured with lower feedrates, a higher volumetric fraction of the interdendritic phase is found.
(3) In the specimens with lower WC% (10 % WC), the variation of the composition of the matrix is residual. Therefore, the feedrate has little effect on the metal-ceramic interaction. Hence, the effect on the overall matrix composition is negligible.

Lastly, the surface hardness of the specimens is mainly defined by the composition of the feedstock. However, the feedrate does affect the mechanical properties of the material to an extent. The interaction term reveals that the effect of the feedrate is not con-

stant throughout the studied experimental domain, as different strengthening mechanisms are present.

(1) When high WC% feedstocks are employed (40 %WC), lower feedrates promote the strengthening of the material. The main strengthening mechanism of these specimens is the solid-solution of tungsten and carbide precipitation. Therefore, the increase of the W% of the matrix promotes carbide precipitation and increases the hardness of the coatings.
(2) When low WC% are employed (10 %WC), higher feedrates result in harder coatings. The main strengthening mechanism of these specimens is grain refinement. Faster processing leads to higher cooling rates. Consequently, the microstructure is refined, and the hardness of the material increases.

Funding

This work was supported by the Basque Government (Eusko Jaurlaritza) [grant number KK-2021/00120 Imagine]; the Spanish Ministry of Science and Innovation [grant numbers PID2019-109220RB-I00 ALASURF, PDC2021-121042-I00 EHU-Coax]; and Business Finland [grant number TANDEM (4056/31/2021)].

CRediT authorship contribution statement

Marta Ostolaza: Conceptualization, Methodology, Formal analysis, Investigation, Writing – original draft. **Jon Iñaki Arrizubieta:** Conceptualization, Investigation, Writing – review & editing, Funding acquisition. **Antoine Queguineur:** Investigation, Writing – review & editing. **Kati Valtonen:** Investigation, Writing – review & editing. **Aitzol Lamikiz:** Conceptualization, Writing – review & editing, Funding acquisition. **Iñigo Flores Ituarte:** Methodology, Resources, Writing – review & editing.

Data availability

Data will be made available on request.

Declaration of Competing Interest

The authors declare that they have no known competing financial interests or personal relationships that could have appeared to influence the work reported in this paper.

Acknowledgements

This work made use of the Tampere Microscopy Center facilities at Tampere University.

Data availability

The data required to reproduce the findings of this study will be made available from the corresponding author on request.

References

[1] K. Holmberg, A. Erdemir, Influence of tribology on global energy consumption, costs and emissions, Friction. 5 (3) (2017) 263–284, https://doi.org/10.1007/s40544-017-0183-5.
[2] European Commission, Sustainable Development Goals, (n.d.). https://ec.europa.eu/international-partnerships/sustainable-development-goals_en (accessed April 7, 2022).
[3] X. Sun, J. Zhang, W. Pan, W. Wang, C. Tang, Research progress in surface strengthening technology of carbide-based coating, J. Alloys Compd. 905 (2022), https://doi.org/10.1016/j.jallcom.2022.164062 164062.
[4] B. Blakey-Milner, P. Gradl, G. Snedden, M. Brooks, J. Pitot, E. Lopez, M. Leary, F. Berto, A. du Plessis, Metal additive manufacturing in aerospace: A review, Mater. Des. 209 (2021), https://doi.org/10.1016/j.matdes.2021.110008 110008.
[5] M.L. Griffith, M.T. Ensz, J.D. Puskar, C.V. Robino, J.A. Brooks, J.A. Philliber, J.E. Smugeresky, W.H. Hofmeister, Understanding the Microstructure and Properties of Components Fabricated by Laser Engineered Net Shaping (LENS), MRS Online Proc. Libr. 625 (2000) 9, https://doi.org/10.1557/PROC-625-9.
[6] Z. Zhang, R. Kovacevic, Laser cladding of iron-based erosion resistant metal matrix composites, J. Manuf. Process. 38 (2019) 63–75, https://doi.org/10.1016/j.jmapro.2019.01.001.
[7] P. Wu, C.Z. Zhou, X.N. Tang, Microstructural characterization and wear behavior of laser cladded nickel-based and tungsten carbide composite coatings, Surf. Coat. Technol. 166 (1) (2003) 84–88, https://doi.org/10.1016/S0257-8972(02)00730-2.
[8] D.P. Karmakar, G. Muvvala, A.K. Nath, High-temperature abrasive wear characteristics of H13 steel modified by laser remelting and cladded with Stellite 6 and Stellite 6/30% WC, Surf. Coat. Technol. 422 (2021), https://doi.org/10.1016/j.surfcoat.2021.127498 127498.
[9] G. Gong, J. Ye, Y. Chi, Z. Zhao, Z. Wang, G. Xia, X. Du, H. Tian, H. Yu, C. Chen, Research status of laser additive manufacturing for metal: a review, J. Mater. Res. Technol. 15 (2021) 855–884, https://doi.org/10.1016/j.jmrt.2021.08.050.
[10] Y. Wu, Y. Liu, H. Chen, Y. Chen, H. Li, X. Cao, Developing the ductility and thermal fatigue cracking property of laser-deposited Stellite 6 coatings by adding titanium and nickel, Mater. Des. 162 (2019) 271–284, https://doi.org/10.1016/j.matdes.2018.11.063.
[11] D. Svetlizky, M. Das, B. Zheng, A.L. Vyatskikh, S. Bose, A. Bandyopadhyay, J.M. Schoenung, E.J. Lavernia, N. Eliaz, Directed energy deposition (DED) additive manufacturing: Physical characteristics, defects, challenges and applications, Mater. Today. 49 (2021) 271–295, https://doi.org/10.1016/j.mattod.2021.03.020.
[12] D.R. Feenstra, R. Banerjee, H.L. Fraser, A. Huang, A. Molotnikov, N. Birbilis, Critical review of the state of the art in multi-material fabrication via directed energy deposition, Curr. Opin. Solid State Mater. Sci. 25 (2021), https://doi.org/10.1016/j.cossms.2021.100924 100924.
[13] ASTM F3187-16 Standard Guide for Directed Energy Podeisiton of Metals, n.d. 10.1520/F3187-16.
[14] E.M. Parsons, S.Z. Shaik, Additive manufacturing of aluminum metal matrix composites: Mechanical alloying of composite powders and single track consolidation with laser powder bed fusion, Addit. Manuf. 50 (2022), https://doi.org/10.1016/j.addma.2021.102450 102450.
[15] T. DebRoy, H.L. Wei, J.S. Zuback, T. Mukherjee, J.W. Elmer, J.O. Milewski, A.M. Beese, A. Wilson-Heid, A. De, W. Zhang, Additive manufacturing of metallic components – Process, structure and properties, Prog. Mater. Sci. 92 (2018) 112–224, https://doi.org/10.1016/j.pmatsci.2017.10.001.
[16] H. Wang, W. Liu, Z. Tang, Y. Wang, X. Mei, K.M. Saleheen, Z. Wang, H. Zhang, Review on adaptive control of laser-directed energy deposition, Opt. Eng. 59 (2020) 1, https://doi.org/10.1117/1.oe.59.7.070901.
[17] D. Lewis, In Situ Reinforcement of Metal Matrix Composites, Met. Matrix Compos. ; Process. Interfaces. (1991) 121–150. https://cir.nii.ac.jp/crid/1570291224191001856.bib?lang=en (accessed May 23, 2022).
[18] G. Wang, J. Zhang, R. Shu, S. Yang, High temperature wear resistance and thermal fatigue behavior of Stellite-6/WC coatings produced by laser cladding with Co-coated WC powder, Int. J. Refract. Met. Hard Mater. 81 (2019) 63–70, https://doi.org/10.1016/j.ijrmhm.2019.02.024.
[19] D. Bartkowski, G. Kinal, Microstructure and wear resistance of Stellite-6/WC MMC coatings produced by laser cladding using Yb:YAG disk laser, Int. J. Refract. Met. Hard Mater. 58 (2016) 157–164, https://doi.org/10.1016/j.ijrmhm.2016.04.017.
[20] D. Bartkowski, A. Bartkowska, Wear resistance in the soil of Stellite-6/WC coatings produced using laser cladding method, Int. J. Refract. Met. Hard Mater. 64 (2017) 20–26, https://doi.org/10.1016/j.ijrmhm.2016.12.013.
[21] G. Muvvala, D. Patra Karmakar, A.K. Nath, Monitoring and assessment of tungsten carbide wettability in laser cladded metal matrix composite coating using an IR pyrometer, J. Alloys Compd. 714 (2017) 514–521, https://doi.org/10.1016/j.jallcom.2017.04.254.
[22] Y. Hu, W. Cong, A review on laser deposition-additive manufacturing of ceramics and ceramic reinforced metal matrix composites, Ceram. Int. 44 (17) (2018) 20599–20612, https://doi.org/10.1016/j.ceramint.2018.08.083.
[23] J. Nurminen, J. Näkki, P. Vuoristo, Microstructure and properties of hard and wear resistant MMC coatings deposited by laser cladding, Int. J. Refract. Met. Hard Mater. 27 (2) (2009) 472–478, https://doi.org/10.1016/j.ijrmhm.2008.10.008.
[24] R. Adam, A. Botes, G. Corderley, Metal matrix composite laser metal deposition for ballistic application, IOP Conf. Ser. Mater. Sci. Eng. 430 (2018), https://doi.org/10.1088/1757-899X/430/1/012001.
[25] N. Li, W. Liu, Y. Wang, Z. Zhao, T. Yan, G. Zhang, H. Xiong, Laser Additive Manufacturing on Metal Matrix Composites: A Review, Chinese J. Mech. Eng. (English Ed. 34 (2021), https://doi.org/10.1186/s10033-021-00554-7.
[26] I. Smolina, K. Kobiela, Characterization of wear and corrosion resistance of stellite 6 laser surfaced alloyed (Lsa) with rhenium, Coatings. 11 (2021) 1–16, https://doi.org/10.3390/coatings11030292.
[27] Y. Ning, P.C. Patnaik, R. Liu, M.X. Yao, X.J. Wu, Effects of fabrication process and coating of reinforcements on the microstructure and wear performance of

Stellite alloy composites, Mater. Sci. Eng. A. 391 (1-2) (2005) 313–324, https://doi.org/10.1016/j.msea.2004.08.083.
[28] A. Mostafaei, A. Heidarzadeh, D. Brabazon, Production of Metal Matrix Composites Via Additive Manufacturing, Encycl. Mater. Compos. (2021) 605–614, https://doi.org/10.1016/B978-0-12-803581-8.11884-3.
[29] M. Zhong, W. Liu, K. Yao, J.-C. Goussain, C. Mayer, A. Becker, Microstructural evolution in high power laser cladding of Stellite 6+WC layers, Surf. Coat. Technol. 157 (2-3) (2002) 128–137, https://doi.org/10.1016/S0257-8972(02)00165-2.
[30] D. Deschuyteneer, F. Petit, M. Gonon, F. Cambier, Processing and characterization of laser clad NiCrBSi/WC composite coatings - Influence of microstructure on hardness and wear, Surf. Coatings Technol. 283 (2015) 162–171, https://doi.org/10.1016/j.surfcoat.2015.10.055.
[31] S. Zhao, C. Jia, Y. Yuan, L. Wang, Y. Huang, L. Yang, Insights into microstructural evolution and dissolution characteristics of reinforced particles in tungsten carbide-nickel composite coatings prepared by laser hot-wire deposition, Int. J. Refract. Met. Hard Mater. 103 (2022), https://doi.org/10.1016/j.ijrmhm.2021.105720 105720.
[32] S. Zhao, S. Xu, L. Yang, Y. Huang, WC-Fe metal-matrix composite coatings fabricated by laser wire cladding, J. Mater. Process. Technol. 301 (2022), https://doi.org/10.1016/j.jmatprotec.2021.117438 117438.
[33] Oerlikon Metco, Material Product Data Sheet. Cobalt Chromium [Nickel Tungsten Silicon] Carbon Alloy Products (Similar to Stellite, Ultimet, Mar M 509), n.d. https://www.oerlikon.com/ecoma/files/DSM-0218.4_CoSuperalloy_StelliteType.pdf?download=true (accessed April 28, 2022).
[34] Oerlikon Metco, Material Product Data Sheet. Spherical Cast Tungsten Carbide Powder for Laser Cladding, n.d. https://www.oerlikon.com/ecoma/files/DSM-0293.0_WC_LC.pdf?download=true (accessed June 2, 2022).
[35] Haynes International, Certification of tests. Stellite(R) Alloy 6-B Plate, 2020.
[36] D. Svetlizky, B. Zheng, A. Vyatskikh, M. Das, S. Bose, A. Bandyopadhyay, J.M. Schoenung, E.J. Lavernia, N. Eliaz, Laser-based directed energy deposition (DED-LB) of advanced materials, Mater. Sci. Eng. A. 840 (2022), https://doi.org/10.1016/j.msea.2022.142967.
[37] J. Nerz, B. Kushner, A. Rotolico, Microstructural evaluation of tungsten carbide-cobalt coatings, J. Therm. Spray Technol. 1 (2) (1992) 147–152, https://doi.org/10.1007/BF02659015.
[38] ISO 6507-1:2018 Metallic Materials - Vickers hardness test - Part 1: Test method., n.d.
[39] A. Farnia, F. Malek Ghaini, J.C. Rao, V. Ocelík, J.T.M. De Hosson, Tantalum-modified Stellite 6 thick coatings: Microstructure and mechanical performance, J. Mater. Sci. 48 (2013) 140–149, https://doi.org/10.1007/s10853-012-6805-4.
[40] D. Klarstrom, P. Crook, J. Wu, Metallography and Microstructures of Cobalt and Cobalt Alloys, Metallogr. Microstruct. 9 (2004) 0. 10.31399/asm.hb.v09.a0003771.
[41] A. Bandyopadhyay, K.D. Traxel, J.D. Avila, I. Mitra, S. Bose, CoCr Alloys, Biomater. Sci. (2020) 257–269, https://doi.org/10.1016/B978-0-12-816137-1.00020-9.